Colossal photovoltages in strain-driven crystal field transition and symmetry breaking of superconducting epitaxial systems

Fei Xiong,[1,2,*] Lin Xie,[3] Luran Zhang,[1] Jiyang Xie,[1] Hui Zhang,[4] Zuimin Jiang,[2] Qingming Chen,[4] and Wanbiao Hu[1,†]

[1]*Key Laboratory of LCR Materials and Devices of Yunnan Province, School of Materials Science and Engineering, Yunnan University, Kunming 650091, People's Republic of China*

[2]*State Key Laboratory of Surface Physics and Department of Physics, Fudan University, Shanghai 200433, People's Republic of China*

[3]*Department of Physics, Southern University of Science and Technology, Shenzhen 518055, People's Republic of China*

[4]*Faculty of Materials Science and Engineering, Kunming University of Science and Technology, Kunming 650093, People's Republic of China*

(Received 14 February 2019; revised manuscript received 17 April 2019; published 14 May 2019)

Materials showing light-induced voltages (LIVs) are a flourishing class characterized by anisotropic charge transport. The LIVs' functionality could be tuned by local perturbations and structural symmetry, but achieving large LIVs is still challenging and a clear guiding principle to this end thus remains to be established. Here, a long-range lattice strain approach that enables manipulating the crystal field and symmetry breaking is proposed to realize colossal LIVs. The tailored tensile and compressive strains are introduced into superconducting $(La_{1.45}Nd_{0.4})Sr_{0.15}CuO_4$ epitaxial films that are fabricated by the pulsed laser deposition method. The experimental characterization indicates that long-range lattice compressive strain results in the epitaxially mosaic structures and the local crystal field transition from tetragonal to octahedral configurations that spontaneously breaks the symmetry. Such a structural transition and change through modulated compressive strain could greatly favor in-plane transport that contributes to a large anisotropy of the Seebeck coefficient ΔS of over 100 μV K^{-1}, achieving strikingly colossal LIVs of over 70 V, many times larger than those of existing materials reported. This would broaden LIVs' promising application in light or photovoltage response and also exemplifies a steady route to exploring new high-performance LIV materials with structural or transport anisotropy.

DOI: 10.1103/PhysRevMaterials.3.054803

I. INTRODUCTION

The light-induced voltage (LIV) phenomenon, discovered decades ago, only occurs in anisotropically thermoelectric films grown on vicinal-cut substrates [1–3]. This is naturally subject to an atomic-layer thermopile (ALT) model that asserts that the voltage signals originate from the off-diagonal term of the Seebeck tensor [4,5]. LIV is thus positively correlated with the anisotropy of the Seebeck coefficient ΔS. The ideal material system for high-performance LIV devices is bound to electronic transport anisotropy [6], regardless of isotropically cubic structured materials, e.g., $SrTi_{1-x}Nb_xO_3$, also exhibiting an LIV of over 6 V with high $\Delta S \sim 25\,\mu$V K^{-1} [7]. Being anisotropic in charge transport, those strongly correlated systems, e.g., the earliest $YBa_2Cu_3O_{7-\delta}$ (YBCO) [1,2], subsequently $La_{1-x}Ca_xMnO_3$ (LCMO) [8,9], and more recently $Ca_3Co_4O_9$ [10], with charge and orbital ordering, electronic phase separation, and superconducting-plane decoupling, usually enable generating LIV effects, making LIV relatively universal and quite appealing.

The materials possessing large and fast-response LIV effects are sought after in a large variety of applications, such as transducers, infrared detectors, and passive devices, that can be operated in ambient environments without bias being involved [11–13]. Unfortunately, the LIV materials developed extensively, e.g., superconductors or magnetoresistive materials, suffer from a common issue; i.e., the LIV is only several volts [14–16]. In spite of the intense activity focused on electron-correlated compounds or something beyond, significant progress in achieving higher LIV is still quite lacking and challenging. There is a predicament currently in that no material shows high LIV and no mechanism shows a potential to bring about a high-LIV property.

Charge transport in the large LIV achieved always regards interactions of electrons, atoms, phonons, and local structures, e.g., defects and strains, as these usually refer to the d/f-electron systems, but some of their key properties remain poorly understood at a fundamental, atomistic level. For example, an atomic-layer thermopile can give a gain of 10^5 to the thermopower, showing an LIV of over 20 V in layered Ca_xCoO_2 [17], but the extent of the correlation to structural tuning and atomic-scale strategy for exploring higher LIV is still at an empirical level.

Detectable LIVs have been demonstrated in topical $La_{2-x}Sr_xCuO_4$ (LSCO) thin films, regardless of being only of several volts [15]. In these layered superconducting thin films, the anisotropy of the Seebeck coefficient may be due to the electronic restriction within the CuO_2 plane, with charge transport along the c direction being dominated by the electronic coupling. Thus, further enhanced structural and transport anisotropy in terms of the electronic location and decoupling the CuO_2 planes is necessary and promising in order to increase LIVs. As Nd doping in LSCO would lead to the charge stripes in CuO_2 planes that enhance electronic

*Corresponding author: f_xiong888@163.com
†huwanbiao@ynu.edu.cn

decoupling between CuO_2 planes [18,19], larger LIVs are expected to be detected in $(La, Nd)_{2-x}Sr_xCuO_4$ films. However, it is only recently that we presented a high LIV $\sim$ 50 V in terms of the enhanced bidimensionality that accelerates the decoupling of the CuO_2 plane in Nd-doped cuprates [6]. Needless to say, we are far from the end of the beginning.

When electronic transport refers to 3*d*-electron systems, it is important to emphasize the crystal field that is correlated with chemical coordination, electrons, spins, and orbitals, which is expected to be changing if physical and chemical modifications [20], e.g., arising from lattice strain engineering, are applied [21–24]. Strain has induced local perturbations in $SrMnO_3$ films with coupling of electrical polarization and structural defects [25], and also in some cases epitaxial strain could break the degeneracy of $3de_g$ and t_{2g} orbitals, thus favoring a particular orbital filling with consequences for functional properties including electronic transport as well as fabricating artificial chemical and magnetic structure [21,26]. Bearing this in mind, we propose a strain-engineering strategy for realizing colossal LIVs in superconducting $(La_{1.45}Nd_{0.4})Sr_{0.15}CuO_4$ (LNSCO) epitaxial thin films, that is, long-range lattice compressive strain, demonstrating the roles in tailoring the crystal field, symmetry breaking, electronic band structures, etc., in order to maximally enhance the anisotropic electronic transport and enhance the LIVs in 3*d*-electron systems.

II. EXPERIMENT

In order to grow high-quality LNSCO epitaxial thin films, polycrystalline LNSCO targets in single phase were synthesized by the solid state reaction method first. Starting material La_2O_3, Nd_2O_3, $SrCO_3$, and CuO powders in stoichiometry were well mixed and milled, and then calcined at 900 °C for 6 h. Thereafter, the mixture was thoroughly ground and pressed into pellets, which were sintered at 1100 °C for 24 h in air to get the final LNSCO targets. The synthesized LNSCO targets demonstrated high density and were in a pure tetragonal phase examined by x-ray diffraction (XRD) (Fig. S1 of the Supplemental Material [27]).

Four single-crystal substrates with the (001)-oriented surface tilted by an angle β toward the [100] direction, i.e., $NdCaAlO_4$ (NCAO), $LaSrAlO_4$ (LSAO), $LaAlO_3$ (LAO), and $SrTiO_3$ (STO), were selected to grow the strained LNSCO epitaxial thin films through the pulsed laser deposition (PLD) method. During the film growth, the distance between the target and the substrate was set to 5 cm. The KrF excimer laser with a wavelength of 248 nm was used to ablate the stoichiometric polycrystalline targets. The energy per laser pulse was 400 mJ and the pulse duration was 28 ns. The laser repeating frequency was kept at 5 Hz and the dynamic oxygen pressure was kept at 60 Pa. The produced energetic particles deposited on the substrate surface formed the films at 880 °C. In order to avoid oxygen nonstoichiometry and increase the crystallization, the as-grown films experienced a subsequent annealing at 800 °C with static oxygen pressure of 2000 Pa for 30 min before cooling to room temperature. The final LNSCO epitaxial thin films were thus obtained.

The crystal structure and phase of the LNSCO films were characterized by x-ray diffraction (XRD; Rigaku TTR18kW) with Cu Kα radiation. The thickness and morphology of the LNSCO films were examined by scanning electron microscopy (SEM; FEI Quanta 200). The interfacial states and atomic-structure information were observed by high-resolution scanning transmission electron microscopy (STEM) equipped with a Cs corrector in the condenser lens system (Thermofisher Themis G2 60–300). The film samples used for TEM observation were prepared by using focused ion beam (FIB; FEI Helios Nanolab 600i) milling to thin down the cross-sectional lamella to around 100 nm with an accelerating voltage of 30 kV. The current used was tuned from the maximum 2.5 nA to a small current of 40 pA by fine polishing at an accelerating voltage of 2 kV. The thin cross-sectional TEM lamella was fixed on the two electrodes of the nanochip by Pt deposition in an FIB system. Lattice vibration and phonon modes of the films under different strain states were analyzed by Raman spectroscopy in a back-scattering configuration (Renishaw inVia), which was coupled with a 514.5 nm Ar^+ laser with an output power of 15 mW. We collected the Raman spectra of the LNSCO thin films on four substrates respectively, i.e., LNSCO/STO, LNSCO/LAO, LNSCO/LSAO, and LNSCO/NCAO, as well as of the substrates. Then, the Raman spectrum of each substrate was subtracted from that of LNSCO/substrate. To characterize the charge transport properties of the films, the surface resistivity versus temperature was also measured by the four-probe method.

The measurement setup and process for LIV signals were followed according to our previous report [6]. First, two indium electrodes separated by 2 mm along the tilting direction were deposited on LNSCO film surface for the electric signal measurement. A photosensor with an exposure area of 2×2 mm^2 was placed in a dark metal box in order to shield from electric-magnetic noise. The pulsed laser, after going through an attenuator, was guided to irradiate on the LNSCO film surface to generate photovoltages, i.e., laser-induced voltages (LIVs). The laser irradiation duration was originally set to 28 ns. The LIV signals were monitored by a time-resolution oscilloscope with 100 MHz bandwidth and 1 MΩ input impedance to obtain the LIV wave forms at room temperature.

III. RESULTS AND EVALUATION

A. Material selection and long-range strain strategy

We explored the possibility of realizing large light/laser-induced voltages by taking a superconducting material, i.e., $(La_{1.45}Nd_{0.4})Sr_{0.15}CuO_4$ (LNSCO), featured with intrinsically two-dimensional CuO_2 structure in the *ab* plane (the structure of LNSCO bulk can be seen in Fig. S1 of the Supplemental Material [27]). The properties of such types of materials are mainly determined by the in-plane transport that can be controlled by the physical and chemical structural modulation. We present herein a physical strategy that is to tune the long-range lattice strain to change the crystal field and spontaneously break the symmetry [Figs. 1(a) and 1(b)]. Driven by the half filling of e_g orbitals, the lattice strain, similarly to the Jahn-Teller (JT) distortion induced by electron-phonon coupling in the M_eO_6 octahedral configuration [21], could

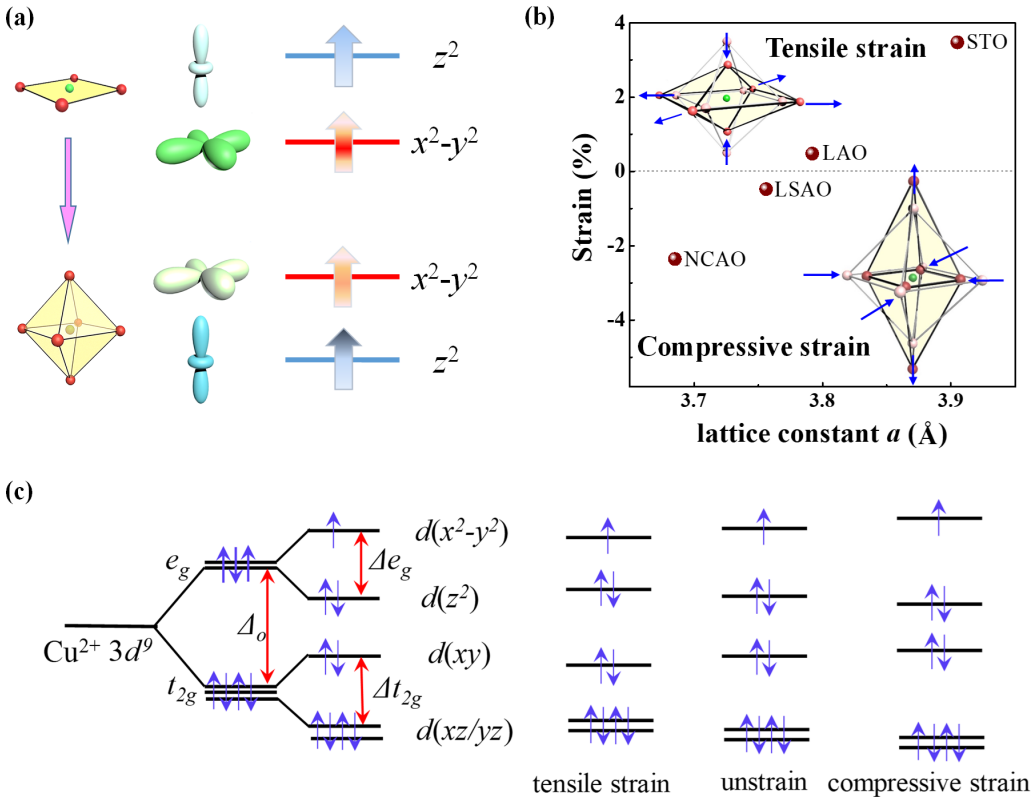

FIG. 1. (a) Representation of the symmetry breaking causing different occupation of the orbitals and e_g energy levels in CuO_2. (b) The calculated stain in the films grown on four different substrates, i.e., NCAO, LSAO, LAO, and STO. The insets show the relative displacement of the oxygen atoms in the CuO_6 octahedron. The green and red circles represent Cu and O atoms, respectively, and the original positions of oxygen atoms are denoted by light red circles. The arrows indicate the shifting directions of atoms under strain. (c) Sketch of energy levels of a Cu^{2+} $3d^9$ cation on the effect of the tetragonal symmetry crystal field, and the effect of both compressive and tensile strains. The gap is expected to be reduced for the compressive strain case.

shift the relative position for the $x^2 - y^2$ and z^2 orbitals and change the orbital filling [Figs. 1(a) and 1(c)] [21,28].

In order to create and modulate the lattice strain properly, four inclined single-crystal substrates, i.e., NCAO, LSAO, LAO, and STO, with the (001)-oriented surface tilted toward the [100] direction were selected, with their cell parameters a (tetragonal structure) in a sequence of $a_{NCAO} < a_{LSAO} < a_{LNSCO} < a_{LAO} < a_{STO}$. The LNSCO films were grown epitaxially on the substrates by the well-tailored pulsed laser deposition (PLD) method and with the surface also tilted by an angle β. Systematic strain was produced and tuned by the film-interfacial lattice mismatch and heterojunction.

B. Identification of the interfacial strain and misorientation

The behaviors, e.g., energy level configurations and splitting of the crystal field, are determined by the local chemical bonding, which is influenced especially by the interfacial states and long-range orientation for the epitaxial systems [29]. To these, high-angle annular dark field scanning transmission electron microcopy (HAADF-STEM) was performed. Normal and very sharp interfaces were observed for the epitaxial films with tensile strain, e.g., the LNSCO-LAO film (Fig. 2(a) and Fig. S2 of the Supplemental Material [27]) that also exhibits regular atomic arrangement in the long range. However, there extensively exists interfacial mismatch for the epitaxial films with compressive strain, in addition to regular atomic order [Fig. 2(e)]. This aspect is mainly embodied in the interfacial atomic/ionic diffusion [Fig. 2(c)] and antiphase stacking [Fig. 2(d)], in which it is experienced through almost a dozen atomic layers. More than this, there are obvious dark contrasts under bright-field observations in LNSCO/NCAO epitaxial films, which demonstrates a good epitaxial quality by selected-area electron diffraction (SAED) (see Fig. S3). These contrasts are associated with the small misalignments between neighboring crystalline regions that are induced by the lattice mismatch originally from interfacial strains. The SAED also reveals that the in-plane lattice constant of the film is ~2% larger that of the NCAO substrate. As a result, a mosaic grain structure with small misoriented crystals is expected in order to relax the interfacial strain.

C. Crystal field transition induced by long-range strain

Figure 3(a) clearly shows that only the sharp (00l) diffraction peaks from LNSCO films and substrates were detected, indicating that all these films epitaxially grow in the c-axis direction and crystallize in a single-phase, tetragonal structure with the space group of $I4/mmm$ without any impurity. Especially, these (00l) diffraction peaks gradually shift toward lower 2θ angles as the films grow on STO, LAO, LSAO, and NCAO, respectively, clear evidence that the out-of-plane

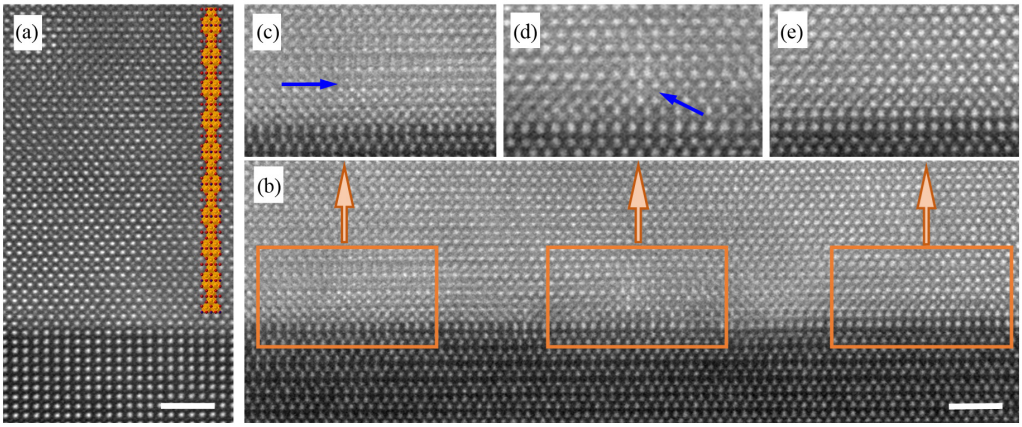

FIG. 2. (a) HAADF images of a tensile-strained film, i.e., LNSCO/LAO. A clear and sharp interface and regular and long-range atomic order are presented, giving the La/Nd/Sr-O polyhedron arrangement accordingly (inset). (b) HAADF images of a compressive-strained film, i.e., LNSCO/NCAO. Obvious interfacial mismatch with different strain regions is observed as highlighted by rectangles, which are directed to the enlarged images in (c)–(e). As analyzed, the image in region (c) mainly reveals the interfacial atomic/ionic diffusion (arrow), (d) gives the antiphase stacking information (arrow), while (e) shows the normal and regular atomic ordering, but with slight elongation in the lattice c axis combined with SAED determination (Fig. S3). The scale bars in (a) and (b) denote 2 nm.

cell parameter c increases accordingly. The c values were calculated with the sequence in $c_{NCAO} > c_{LSAO} > c_{LNSCO} > c_{LAO} > c_{STO}$ [Fig. 3(a)]. Bond valence sum (BVS) calculations indicate that Cu would release the charges toward the c-axis orientation because Cu in the ab plane is seriously overbonded for the LNSCO grown on LSAO and NCAO substrates, forming a quasi-six-coordination, while opposite charge-releasing behaviors for the LAO and STO counterparts still maintain the planar or tetragonal coordination. Along with the change in locally charge releasing and chemical coordination, the local energy configuration would have a transition from the tetragonal crystal field to the octahedral crystal field. Thus, the two types of long-range lattice strain vary the local crystal field, i.e., the octahedral field under compressive strain but the tetragonal field under tensile strain, as predicted in Fig. 1(b).

The state change in crystal field is definitely correlated to the structural anisotropy induced by the increased interlayer spacing of the adjacent conducting layers, i.e., CuO_2 planes. The anisotropic parameters (γ^2) in high-T_c superconducting cuprates would increase with the spacing of the two-dimensional (2D) CuO_2 planes [6,30]. And then, the crystal field transition would accelerate the decoupling of the adjacent conducting layers, i.e., CuO_2 planes that directly

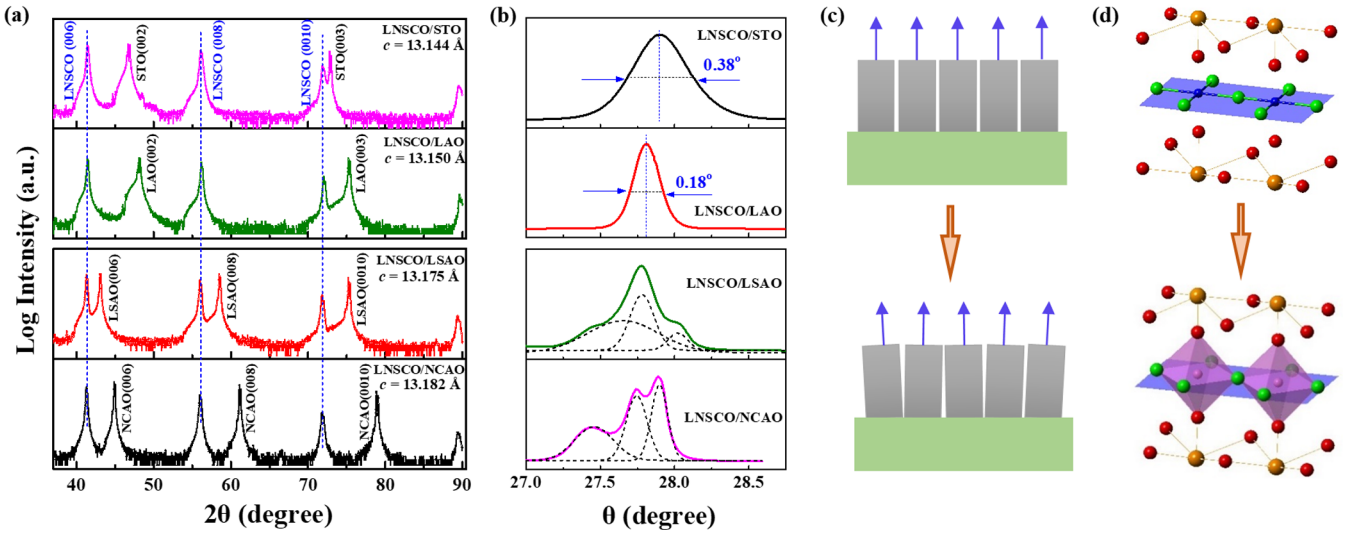

FIG. 3. (a) XRD characterizations for the LNSCO epitaxial films deposited on STO, LAO, LSAO, and NCAO substrates, respectively, with tilting angle $\beta = 15^\circ$. All the films show a (001) orientation in high quality. (b) XRD rocking curves of LNSCO (008) reflection lines as well as the fitting results. It is revealed that compressive strain could induce a mosaic structure while tensile strain simply broadens the rocking curves. (c) Illustration of structural orientation from a normal to mosaic structure for LNSCO films. Local orientation differing but with long-range ordering indicates the mosaic structures with existing lattice strains. (d) Local crystal structural transition from plane/tetragonal coordination into octahedral coordination under strain.

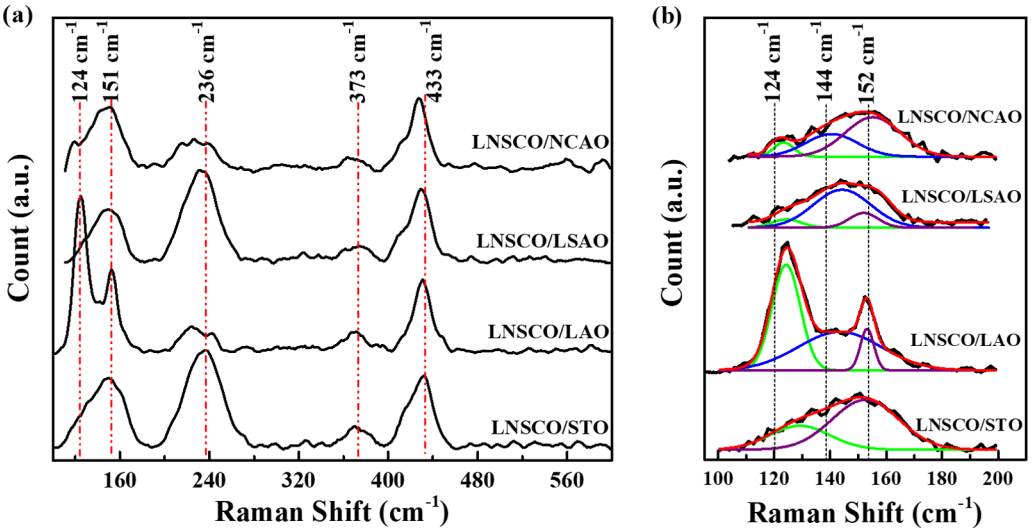

FIG. 4. (a) Raman spectra of LNSCO epitaxial films grown on four substrates of NCAO, LSAO, LAO, and STO. There are apparent differences in the main Raman peaks' positions (denoted by dashed lines) for different substrate counterparts. (b) Enlarged Raman characteristics and corresponding Lorenz fitting curves in the range of 100–200 cm^{-1}. The fitting indicates the existence of three lattice vibration peaks located at 124 cm^{-1}, 144 cm^{-1}, and 152 cm^{-1} (denoted by dashed lines), respectively.

impose great influences on the charge transport [6]. Measurements of resistivity versus temperature $\rho(T)$ reveal that the LNSCO thin films grown under compressive strain exhibit enhancement of the superconducting transition temperature T_c and metallic transport properties (Fig. S4 of the Supplemental Material [27]). Simultaneously, the film grown under tensile strain shows an obvious upturn in the curve as the temperature is reduced, before the onset of superconductivity. Such a behavior has been observed for the underdoped "214" cuprate compound [31,32]. But the film grown under compressive strain shows a linear $\rho(T)$, which is usually observed for optimally doped compounds [31,32]. Considering that the electronic behaviors in the CuO_2 plane dominate the charge transport in these layered compounds, the phenomena seem to suggest that electronic location within the CuO_2 plane should be enhanced, while electronic transport by coupling among CuO_2 should be suppressed, as LNSCO films are grown under compressive strain.

The occurrence of crystal field transition would usually result in the symmetry breaking in orbital energy configurations as well as the long-range structure. Evidence of symmetry breaking induced by the long-range lattice strain is the observation of mosaic structure in compressively stained films revealed by the rocking curve of LNSCO (008) reflection peaks [Fig. 3(b)]. The whole single crystal is likely "divided" into small pieces whose crystal orientations are not exactly coincident. This mosaicity involves a substructure in which neighboring regions are oriented slightly differently or with coexistence of the orientation-differing domains [Fig. 3(c)] [33], consistent with TEM observations. The mosaic rocking curve for LNSCO films on LSAO and NCAO substrates can be fitted into three peaks, including two side peaks close to the maximum intensity peak, which likely breaks the long-range crystal periodicity that permits the tilting order of CuO_6 octahedra. It is worth noting that larger compressive strain leads to more obvious mosaic structures, while larger tensile strain just makes the rocking curve broaden.

D. Phonon vibrations and long-range symmetry breaking

To obtain a better insight into the structural nature, Raman back-scattering spectroscopy [Figs. 4(a) and 4(b)] was carried out. Vibrations of Cu atoms make only ungerade modes, and the A_{1g} and E_g optical modes are Raman active for the tetragonal primitive cell including one molecular unit [34]. Two obvious phonons situated at 236 cm^{-1} and 433 cm^{-1}, corresponding to the in-phase vibration of the La/Nd/Sr-O_{ap} bond and apical oxygen vibration along the c axis [34–36], slightly shift to a lower energy in the octahedral crystal field configuration. This is an important sign of decreasing ionic interaction in La/Nd/Sr-O bonding, similar to that in tetragonal $La_{2-x}Sr_xNiO_4$ systems [37], i.e., decoupling between adjacent 2D CuO_2 planes under compressive lattice strain. Because of the asymmetry of the vibration peaks, the spectra in the range of 100–200 cm^{-1} can be fitted into three peaks [Fig. 4(b)]: the mode at 124 cm^{-1} is related to the CuO_6 octahedra rotation while the one at 152 cm^{-1} is assigned to the vibration of the A-site atom (La/Nd) along the [110] direction [34]. The appearance of these two modes (A_g) allowed only for the mid-temperature orthorhombic (space group $Abma$) phase implies a slight orthorhombic distortion that would lower the symmetry. The simultaneous energy change for these two modes is only due to the change in La(Nd)-Cu interaction; that is, compressive lattice strain leads to a decrease for the La(Nd)-Cu interaction [35]. Two additional infrared-dominant B_{2u} modes at 144 cm^{-1} and 373 cm^{-1} are also detected, indicative of the breakup in inversion symmetry that stems from some specific electronic transition coupled with the infrared modes under the long-range lattice strain [34].

It is thus clear that both the long-range translational symmetry and inversion symmetry are broken in the present LNSCO films with forming local symmetry-lowering regions but average tetragonal structure is still maintained. The symmetry-breaking phenomenon reported here is correlated with a manifestation of an "orthorhombic anisotropy" for

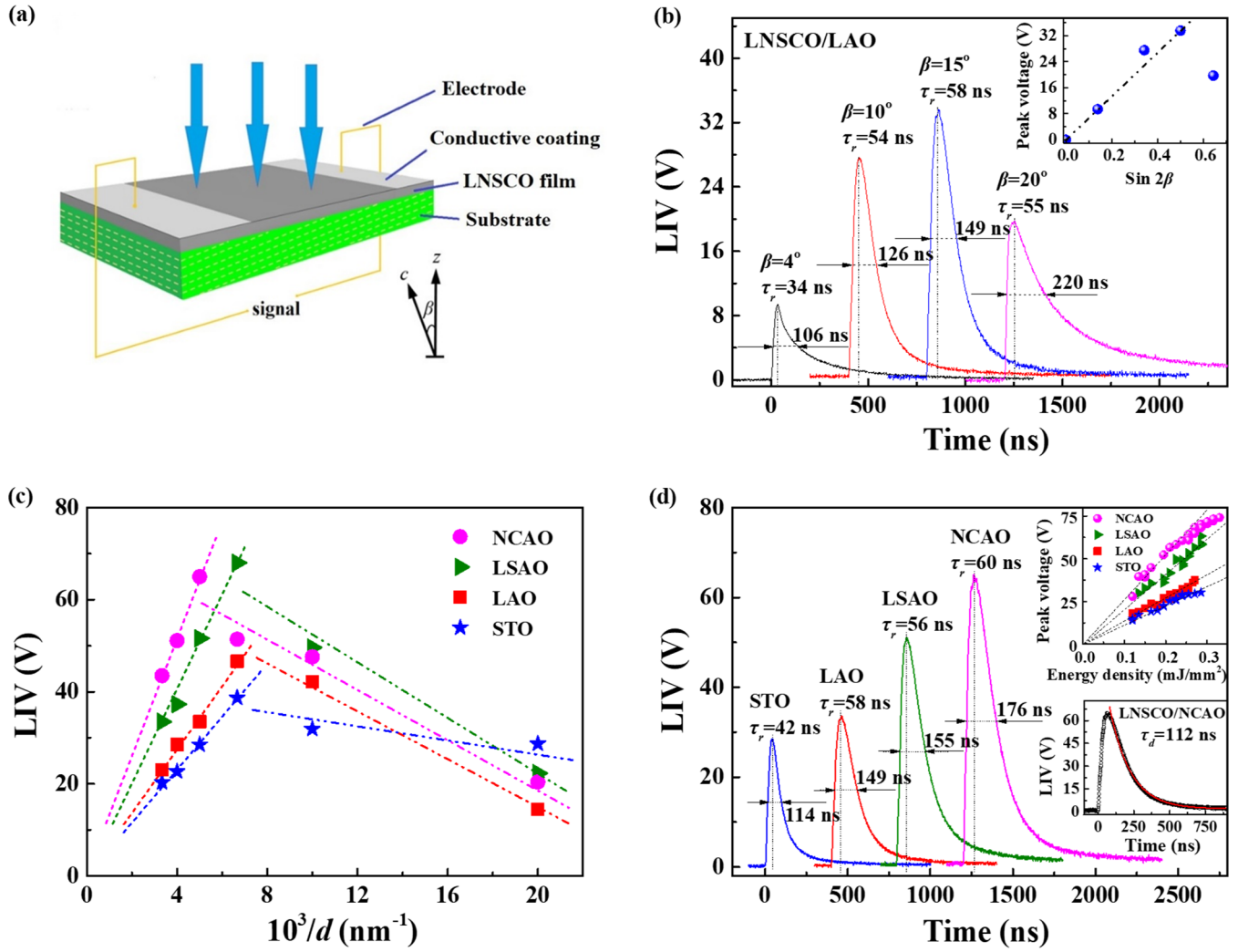

FIG. 5. (a) Schematic measurement for the LIV behaviors of the LNSCO film photosensor. (b) Tilting dependence (angle β) of the LIV signals of 200 nm LNSCO films on LAO substrates. LIV measurements are based on the laser irradiation conditions: wavelength is 248 nm, pulse duration is 28 ns, and energy density per laser pulse is 0.25 mJ mm^{-2}. Inset shows the dependences of summit LIVs versus tilting angle β. (c) Dependencies of summit LIVs versus films' thickness (d^{-1}). The linear relationship between LIVs and d^{-1} can be obtained when the thickness d is beyond 150 nm. (d) LIVs of the 200 nm LNSCO films grown on different substrates. Insets show the dependences of summit LIVs versus energy density of laser irradiations, and the LIV exponential decay behavior of LNSCO film grown on NCAO. Linear relationship (see fitting curves) is demonstrated as expected on the relatively low energy density.

electron transport. It is worth noting that although in-plane anisotropy of electron transport has been anticipated theoretically and dubbed "electronic nematicity" [38], symmetry breaking in terms of orthorhombic anisotropy is yet undetected in optimally doped and overdoped copper oxides. The crystal field transition favoring the formed CuO_6 octahedra tilting under the compressive state likely reduces the transfer integral between the nearest-neighbor Cu $3d(x^2 - y^2)$ orbitals, producing significant charge order and interdomain correlations in CuO_2 layers, by which the in-plane conductance is enhanced [39].

E. Colossal laser-induced voltages

Closely related to anisotropic charge transport under long-range lattice strain, laser-induced voltages (LIVs) for LNSCO films as a function of tilting angles, film thickness, substrates, and laser pulse energy were measured [see Figs. 5(a)–5(d)]. The measurement setup is demonstrated in Fig. 5(a). When the pulsed laser illuminates the same film on the front surface and on the back side, respectively, the inversion of the LIV polarity occurrs as the irradiation direction is reversed (Fig. S5 of the Supplemental Material [27]), indicating that the detected LIV signals on LNSCO films are due to the thermoelectric response from the temperature gradient along the out-of-plane direction of the film [4]. The transverse voltages are correlated with the temperature difference ΔT along the surface normal by irradiation pulse, and the nonzero component in the off-diagonal thermal-electronic coefficient tensor $(S_{ab} - S_c)\sin 2\beta$ [4,5]. The detected LIV signals of LNSCO films vary differently with tilting angles β and are proportional to $\sin 2\beta$ within a certain angle, e.g., $\beta = 15^\circ$ in this work [insets of Fig. 5(b) and Fig. S6], which further manifests that the anisotropy transport properties in these layered materials

TABLE I. Measured and calculated LIV parameters of LNSCO epitaxial films on four different substrates: NCAO, LSAO, LAO, and STO. The measured parameters include tilting angle β, film thickness d, LIV peak voltage V_p, rising time τ_r, decay time τ_d, and response time τ. The calculated parameters are the figure of merit Z, thermal diffusion coefficient D, and anisotropy of thermoelectric power ΔS, which are obtained based on the measured LIVs and atomic-layer thermopile model. LIV measurements are based on the laser irradiation conditions: wavelength is 248 nm, pulse duration is 28 ns, and energy density per laser pulse is 0.25 mJ mm^{-2}. The detailed parameters for the LNSCO films with different thicknesses and tilting angles are also seen in Table S1.

Material				LIV				Calculated data		
Film	Substrate	β (deg)	d (nm)	V_p (V)	τ_r (ns)	τ_d (ns)	τ (ns)	$Z = V_p/\tau_r$ (V ns^{-1})	D (m^2 s^{-1})	ΔS (μV K^{-1})
LNSCO	NCAO	15	200	65.0	60	153	176	1.08	1.06×10^{-7}	102
LNSCO	LSAO	15	200	51.0	56	133	155	0.91	1.22×10^{-7}	85
LNSCO	LAO	15	200	33.5	58	112	149	0.58	1.45×10^{-7}	54
LNSCO	STO	15	200	28.5	42	70.5	114	0.68	2.30×10^{-7}	48

have caused the anisotropic thermoelectric effect and thermal diffusion [2,5].

Strikingly shown in Fig. 5(d), all the LNSCO films exhibit quite large LIVs that are easily beyond a magnitude of 30 V, far higher than any reported before. The LIVs are also improved with relatively high pulse energy [Fig. 5(d), inset]. Colossal peak voltages (V_p) of over 65 V are achieved for the films on LSAO and NCAO substrates by the laser irradiation at an energy density of 0.25 mJ mm^{-2}. Such a V_p is two times larger than that detected on the films grown on the STO substrate, demonstrating the enhanced LIV under the compressive strain.

To obtain more comprehensive insight into the LIV behaviors, the time-response LIV curves were plotted [Figs. 5(b) and 5(d)]. All the films behave with a quick response at the nanosecond level when irradiated by 28 ns laser pulses, which is a typical characteristic of LIV decaying limited by the heat conduction velocity. A one-dimensional heat conduction model considered with time evolution could therefore be used to describe the time-dependent LIVs' behavior [5],

$$V(t) = \frac{\alpha E l \sin(2\beta)}{4d\rho c\sqrt{\pi Dt}}(S_{ab} - S_c)\left(e^{-\frac{\delta^2}{4Dt}} - e^{-\frac{d^2}{4Dt}}\right). \quad (1)$$

Here t is the time, β the tilting angle, d the film thickness, l the exposure length of the photosensitive films, δ the laser penetration depth, and additionally there are other physical natures, e.g., mass density ρ, specific heat c, thermal diffusion constant D, and light absorbance α. S_{ab} and S_c are the Seebeck coefficients in the CuO_2 plane and along the c-axis direction, respectively. The obtained colossal LIVs, as stated above, are linked to structural symmetry breaking as well as the local crystal field transition from tetragonal to octahedral configurations. These structural changes cause the decoupling interactions between adjacent CuO_2 planes that are undermined, and meanwhile, in-plane charges are heavily localized in Cu because of the shortened Cu-O bonds, thus accelerating the anisotropic transport. As a result, the anisotropy of the Seebeck coefficient $\Delta S = S_c - S_{ab}$ would be increased, contributing to the colossal LIVs.

The expected linear relationship between the LIVs and d^{-1} is demonstrated as the thickness beyond 150 nm (Fig. 5(c) and Fig. S7 of the Supplemental Material [27]). The abnormal behaviors of LIVs on the thinner films may be related to the film thickness less than the laser penetration depth, in which the laser irradiation would generate a small temperature difference, thus a smaller LIV [40]. Meanwhile, heat transfer from the film to the substrate would be enhanced in this case, so that establishing uniform temperature needs more time [3], and then LIV decaying is delayed (Fig. S7). These results reveal that the theoretical model can describe the LIV behaviors in LNSCO films precisely just when the film thickness is larger than 150 nm.

Supposing that the voltage decay is mainly due to the thermal diffusion, i.e., the anisotropic transport for the electrons, Eq. (1) can be simplified to a single exponential function $A\exp(-t/\tau_d)$ with two parameters, a pre-exponent constant A and decay time τ_d, to characterize the decay behavior. This function has been also used in tilted Ca_xCoO_2 films with a thermoelectric origin for the LIVs [3]. Fitting the voltage decay curves yields the τ_d listed in Table I. Considering that the response times (rising time τ_r, i.e., the duration in which the LIVs reach peak voltage, and τ_d) have a linear relationship with the film resistance observed in LIV-featured LCMO and YBCO thin films, i.e., $\tau_r = C_r R_e$ and $\tau_d = C_d R_t$, where C_r and C_d have capacitance dimension and R_e and R_t are the electrical resistance and thermal resistance, respectively [41], it can be concluded that LIVs as well as the voltage rising times are associated with the charge accumulation by the electron diffusion/transport in temperature-gradient films. However, the voltage decay is mainly caused by thermal diffusion along the c-axis direction, so the decay time would be determined by thermal resistance of the films. Under this condition, the thermal diffusion coefficient (D) of the films could be estimated from LIV curves (Table I and Table S1 of the Supplemental Material [27]), and shows larger values with the effect of larger tensile strain, while it decreases with increased compressive strain.

In the layered cuprates, the anisotropic transport demonstrates a scene in which charge transport in the CuO_2 planes is in terms of metallic conduction hopping, while nonmetallic conduction is along the c-axis direction [2,15], which thus is correlated with anisotropic thermoelectric properties, inducing a large Seebeck coefficient along the c-axis direction but a small one in the ab plane [15]. The large anisotropy of thermopower $\Delta S = S_c - S_{ab}$ would contribute to the large LIVs in the following format,

$$\Delta S = |S_{ab} - S_c| = \frac{V_p \kappa \sqrt{\pi \tau_0 \tau_d}}{\alpha E l \sin(2\beta)}. \quad (2)$$

ΔS can be calculated as listed in Table I showing a largest value of over 100 μV K^{-1}, provided $\tau_0 = 28$ ns, $l = 2$ mm, thermal conductivity κ adopted from the value reported by Cassart *et al.* [42], and the measured values of V_p, τ_d, and α. It is clear that ΔS increases gradually during the crystal field transition and symmetry-breaking process, always being much higher for the films under larger compressive state. This coincides well with the colossal LIV magnitudes detected in Fig. 5(d), again implying that large anisotropy of electronic structure induced by strain is responsible for high LIVs.

IV. DISCUSSION

To reconcile the correlation physics in crystal field transition and symmetry breaking, we compared the crystal structures and orbital configurations for B-site Cu^{2+} with $3d^9$ under tensile and compressive strain states shown in Figs. 1(a) and 1(c). The tetragonal crystal field splitting leads to a breakup of the e_g orbitals (z^2, $x^2 - y^2$) higher in energy than the t_{2g} orbitals (xy, xz, yz) [23,28]. Further lowering of the crystal field symmetry breaks the degeneracy of z^2 and $x^2 - y^2$ orbitals. A-site Sr doping induces holes in the $d(x^2 - y^2)$ band that is below the Fermi level. The absence of apical oxygen (O_{ap}) coordination in in-plane or tetragonal field configurations results in the reduction of the repulsive Cu-3$d(z^2)$ to O-2$p(z)$ electron-electron interaction, which is associated with relatively high in-plane resistivity that impedes the charge transport. This is somewhat similar to $La_{1.85}Sr_{0.15}CuO_4$ [28], an isostructural cuprate, but only presents an order smaller LIV than that of the Nd-doped counterpart here (see Fig. S8 of the Supplemental Material [27]).

It is doubtless that the energy levels of the $x^2 - y^2$ and z^2 orbitals behave distinctly as they are normally reversed under tetragonal and octahedral states, while the octahedral energy configurations, furthermore, would be substantially modified. Long-range lattice compressive strain could move the $d(x^2 - y^2)$ band farther up in energy and increase its bandwidth at the same time [23]. The Fermi surface thus becomes more anisotropic. The difference of the effective mass along the c-axis direction and in the ab plane becomes larger than that in the tensile state. As a result, the conductivity in the ab plane will increase, and the derivative of the density of states will decrease to reduce the thermopower. The Seebeck coefficient correlated with electronic transport also shows a consistent tendency to electronic conductivity under the octahedral state. This is consistent with the preferential orbital occupation expected from the strain from the substrate that has been suggested by the transport and magnetic measurements and the density-functional calculation [21].

V. CONCLUSION

We have identified in detail the multiple-structural couplings responsible for the largest laser-induced voltage (LIV) achieved to date. Colossal LIV of up to 70 V is demonstrated in LNSCO epitaxial film through long-range lattice compressive strain that modulates the local crystal field and symmetry breaking with contributing to the large anisotropy of the Seebeck coefficient favoring enhanced in-plane transport. As capable of a universal strategy, interfacial strain engineering tailoring has demonstrated multiscale couplings in local chemical bonds, orbital electron filling, electronic band structures, and anisotropic states, analogs to such instances addressed before as the multifunctional approach for 2D electronic gas, interfacial superconductors, quasicrystals, artificial chemical and magnetic structure, and ferroelectricity. Considering there are many existing strongly correlated electronic systems involving the electronic structure and local bonding, ordering phenomena, and electron localization variables available, strain-driven crystal field transition and symmetry breaking would similarly open a route for structural modulation in complex oxides to achieve not only the present colossal LIVs but also desirable functions such as magnetization, polarization, and catalysis.

ACKNOWLEDGMENTS

This work was supported by the National Natural Science Foundation of China (Grants No. 11464049, No. 1156402, No. 51702281, and No. 21773205), the Applied Basic Research Foundation of Yunnan Province (Grant No. 2015FB112), the Key R&D program of Yunnan Province (Grant No. 2018BA068), and the Open Project of the Key Laboratory for Surface Physics of Fudan University (Grant No. KF2015-06). W.H. thanks the "One Thousand Youth Talents" Program of China. This work was also supported by the Pico Center at SUSTech, which receives support from the Presidential Fund and the Development and Reform Commission of Shenzhen Municipality.

[1] C. L. Chang, A. Kleinhammes, W. G. Moulton, and L. R. Testardi, Phys. Rev. B **41**, 11564 (1990).
[2] P. X. Zhang and H. U. Habermeier, J. Nanomater. **2008**, 1 (2008).
[3] K. Takahashi, T. Kanno, A. Sakai, H. Adachi, and Y. Yamada, Phys. Rev. B **83**, 115107 (2011).
[4] H. Lengfellner, G. Kremb, A. Schnellbögl, J. Betz, K. F. Renk, and W. Prettl, Appl. Phys. Lett. **60**, 501 (1992).
[5] P. X. Zhang, W. K. Lee, and G. Y. Zhang, Appl. Phys. Lett. **81**, 4026 (2002).
[6] F. Xiong, M. Wang, H. Zhang, L. Xie, C. Guo, J. Shao, Z. Jiang, Q. Chen, and W. Hu, Adv. Electron. Mater. **4**, 1800116 (2018).
[7] Y. Qin, T. Zhao, H. Zhang, B. Wang, P. Zhang, and J. Yang, Appl. Phys. Lett. **102**, 253901 (2013).
[8] H.-U. Habermeier, X. H. Li, P. X. Zhang, and B. Leibold, Solid State Commun. **110**, 473 (1999).
[9] J. Ma, H. Zhang, Q. Chen, and X. Liu, J. Appl. Phys. **114**, 043708 (2013).
[10] S. Song, L. Yu, J. Hu, A. Liu, and Y. Zhong, Appl. Phys. A **123**, 595 (2017).

[11] P. X. Zhang, C. Wang, G. Y. Zhang, L. Yu, W. K. Lee, and H.-U. Habermeier, Opt. Laser Technol. **36**, 341 (2004).

[12] G. Y. Zhang, H. Zhang, S.-L. Tan, P.-X. Zhang, T.-Y. Tseng, H.-U. Habermeier, C.-T. Lin, and P. A. Singjai, Appl. Phys. A **116**, 1033 (2014).

[13] T. Zahner, R. Stoerstorfer, S. Reindl, T. Schauer, A. Penzkofer, and H. Lengfellner, Phys. C (Amsterdam) **313**, 37 (1999).

[14] X. Liu, X. Yin, Q. Chen, H. Zhang, and M. Cao, Mater. Sci. Eng. B **185**, 105 (2014).

[15] F. Xiong, H. Zhang, Z. M. Jiang, and P. X. Zhang, J. Appl. Phys. **104**, 053118 (2008).

[16] L. Zhang, Q. Hua, and Y. Fang, J. Laser Appl. **25**, 052002 (2013).

[17] K. Takahashi, T. Kanno, A. Sakai, H. Adachi, and Y. Yamada, Appl. Phys. Lett. **97**, 021906 (2010).

[18] J. M. Tranquada, B. J. Sternlieb, J. D. Axe, Y. Nakamura, and S. Uchida, Nature (London) **375**, 561 (1995).

[19] E. Berg, E. Fradkin, E.-A. Kim, S. A. Kivelson, V. Oganesyan, J. M. Tranquada, and S. C. Zhang, Phys. Rev. Lett. **99**, 127003 (2007).

[20] X.-Z. Lu and J. M. Rondinelli, Nat. Mater. **15**, 951 (2016).

[21] D. Pesquera, G. Herranz, A. Barla, E. Pelerin, F. Bondino, E. Magnano, F. Sánchez, and J. Fontcuberta, Nat. Commun. **3**, 1189 (2012).

[22] T. L. Meyer, R. Jacobs, D. Lee, L. Jiang, J. W. Freeland, C. Sohn, T. Egami, D. Morgan, and H. Lee, Nat. Commun. **9**, 92 (2018).

[23] V. Pardo, A. S. Botana, and D. Baldomir, Phys. Rev. B **87**, 125148 (2013).

[24] H. Simons, A. B. Haugen, A. C. Jakobsen, S. Schmidt, F. Stöhr, M. Majkut, C. Detlefs, J. E. Daniels, D. Damjanovic, and H. F. Poulsen, Nat. Mater. **17**, 814 (2018).

[25] C. Becher, L. Maurel, U. Aschauer, M. Lilienblum, C. Magén, D. Meier, E. Langenberg, M. Trassin, J. Blasco, I. Krug, P. A. Algarabel, N. A. Spaldin, J. A. Pardo, and M. Fiebig, Nat. Nanotechnol. **10**, 661 (2015).

[26] S. Farokhipoor, C. Magén, S. Venkatesan, J. Íñiguez, C. J. M. Daumont, D. Rubi, E. Snoeck, M. Mostovoy, C. Graaf, A. Müller, M. Döblinger, C. Scheu, and B. Noheda, Nature (London) **515**, 379 (2014).

[27] See Supplemental Material at http://link.aps.org/supplemental/10.1103/PhysRevMaterials.3.054803 for the structures of $(La_{1.45}Nd_{0.4})Sr_{0.15}CuO_4$ bulk and thin films and additional XRD, SEM, TEM, and LIV data.

[28] H. Oyanagi, N. L. Saini, A. Tsukada, and M. Naito, J. Phys. Chem. Solids **67**, 2154 (2006).

[29] G. Shibata, M. Kitamura, M. Minohara, K. Yoshimatsu, T. Kadono, K. Ishigami, T. Harano, Y. Takahashi, S. Sakamoto, Y. Nonaka, K. Ikeda, Z. Chi, M. Furuse, S. Fuchino, M. Okano, J. Fujihira, A. Uchida, K. Watanabe, H. Fujihira, S. Fujihira, A. Tanaka, H. Kumigashira, T. Koide, and A. Fujihira, npj Quantum Mater. **3**, 3 (2018).

[30] J.-i. Shimoyama, K. Kitazawa, K. Shimizu, S. Ueda, S. Horii, N. Chikumoto, and K. Kishio, J. Low Temp. Phys. **131**, 1043 (2003).

[31] J.-P. Locquet, J. Perret, J. Fompeyrine, E. Mächler, J. W. Seo, and G. Van Tendeloo, Nature (London) **394**, 453 (1998).

[32] T. Kimura, S. Miyasaka, H. Takagi, K. Tamasaku, H. Eisaki, S. Uchida, K. Kitazawa, M. Hiroi, M. Sera, and N. Kobayashi, Phys. Rev. B **53**, 8733 (1996).

[33] D. Zeng, W. Jie, T. Wang, G. Zha, and J. Zhang, Nucl. Instrum. Method Phys. Res. A **586**, 439 (2008).

[34] S. Sugai, Phys. Rev. B **39**, 4306 (1989).

[35] S. Nimori, H. Hata, H. Ogita, F. Nakamura, S. Sakita, N. Kikugawa, T. Fujita, and M. Udagawa, Phys. B (Amsterdam) **263–264**, 663 (1999).

[36] S. Nimori, S. Sakita, F. Nakamura, T. Fujita, H. Hata, N. Ogita, and M. Udagawa, Phys. Rev. B **62**, 4142 (2000).

[37] M. Udagawa, T. Yamaguchi, Y. Nagaoka, N. Ogita, M. Kato, Y. Maeno, T. Fujita, and K. Ohbayashi, Phys. Rev. B **47**, 11391 (1993).

[38] S. A. Kivelson, E. Fradkin, and V. J. Emery, Nature **393**, 550 (1998).

[39] S.-i. Shamoto, Phys. C (Amsterdam) **341–348**, 1999 (2000).

[40] F. Xiong, H. Zhang, S. Yang, D. Li, Z. Zhang, and Q. Chen, Appl. Phys. A **120**, 717 (2015).

[41] G. Y. Zhang, P. X. Zhang, H. Zhang, and W. K. Lee, IEEE Sens. J. **8**, 194 (2008).

[42] M. Cassart, J. P. Issi, J. Hejtmánet, C. Brisson-Robin, E. Ben Salem, B. Chevalier, and A. Tressaud, Phys. C (Amsterdam) **259**, 385 (1996).